nature catalysis

Article

https://doi.org/10.1038/s41929-024-01135-2

# Square-pyramidal subsurface oxygen [$Ag_4OAg$] drives selective ethene epoxidation on silver

Received: 21 August 2023

Accepted: 27 February 2024

**Dongxiao Chen[1,4], Lin Chen[1,4], Qian-Cheng Zhao[1], Zheng-Xin Yang[1], Cheng Shang[1,2] & Zhi-Pan Liu[1,2,3]** ✉

Ag-catalysed ethene epoxidation is the only viable route for making ethene oxide (EO) in industry, but the active site remains elusive due to the lack of tools to probe this reaction under high temperature and high-pressure conditions. Here, aided by advanced machine-learning grand canonical global structure exploration and in situ experiments, we identify a unique surface oxide phase, namely $O_5$ phase, grown on Ag(100) under industrial catalytic conditions. This phase features square-pyramidal subsurface O and strongly adsorbed ethene, which can selectively convert ethene to EO. The other Ag surface facets, although also reconstructing to surface oxide phases, only contain surface O and produce $CO_2$. The complex in situ surface phases with distinct selectivity contribute to an overall medium (50%) selectivity of Ag catalyst to EO. Our further catalysis experiments with in situ infra-red spectroscopy confirm the theory-predicted infra-red-active C=C vibration of adsorbed ethene on $O_5$ phase and the microkinetics simulation results.

Ethene epoxidation, a textbook example of kinetically controlled heterogeneous catalysis reactions, holds a central role in the chemical industry, transforming petroleum into valuable chemicals[1–3]. Silver stands out as the sole catalyst contender for selectively making ethene oxide (EO) while suppressing the combustion to $CO_2$ (ref. 4). Despite more than 50 years of research, this important reaction remains highly elusive, particularly on those pertinent to the active phase of Ag catalysts and the origin of the EO selectivity occurring at high-pressure industrial conditions[5–16]. The poor knowledge on the fundamental aspects of the reaction hinders the design of more general epoxidation catalysts for synthesizing alkene (for example, propene) epoxides[17,18].

The query about the active site in Ag catalysts dates back to the 1970s[5,19,20], but was hampered due to the limitation of surface science techniques, typically operating at a maximum of mbar level that is well below the industrial condition (490–550 K, 2 MPa, with $O_2$ and $C_2H_4$ pressures both around 1 bar)[4]. Importantly, the epoxidation selectivity is highly sensitive to $O_2$ and ethene pressures: under the mbar-level, the EO selectivity is generally below 2% (refs. 21,22), substantially lower than the typical 50% selectivity from unpromoted Ag catalysts under high-pressure conditions (>0.1 bar)[23] and up to 80% through facet engineering by increasing the (100) exposure and reducing stepped sites[24,25]. The pressure–gap dilemma thus sparks long-time discussions of the reaction mechanism, for example, regarding the origin of the active oxygen species that are transferred to EO[26]. Via scanning tunnelling microscopy[9–11,21,27–29] and in situ X-ray photoelectron spectroscopy (XPS)[14,16,30,31], the in situ formation of Ag surface oxide phases has been observed, which contain multiple types of oxygen. It was suggested that the surface oxygen species of a 528 eV $O_{1s}$ core-level signal are non-selective to EO[14,32], while that with the 530 eV signal, once hypothesized to be the adsorbed O species on metal Ag[33–36] and recently

---

[1] Collaborative Innovation Center of Chemistry for Energy Materials (iChEM), Shanghai Key Laboratory of Molecular Catalysis and Innovative Materials, Key Laboratory of Computational Physical Science, Department of Chemistry, Fudan University, Shanghai, China. [2] Shanghai Qi Zhi Institution, Shanghai, China. [3] Key Laboratory of Synthetic and Self-Assembly Chemistry for Organic Functional Molecules, Shanghai Institute of Organic Chemistry, Chinese Academy of Sciences, Shanghai, China. [4] These authors contributed equally: Dongxiao Chen, Lin Chen. ✉e-mail: zpliu@fudan.edu.cn

attributed to traces of sulfur ($SO_4$ units)[16,37], was long suspected to be the oxygen source of EO product. There are also other oxygen species, such as subsurface O with $O_{1s}$ signal of ~529 eV (refs. 14,15,30), but their catalytic roles are largely unknown[13]. Apparently, no conclusive atomic picture is now available for interpreting all existing experimental observations, which is largely because the active Ag (surface oxides) phases are only present under high-pressure catalytic conditions. The Ag metal and surface oxides identified under low-pressure experimental conditions are both found to be not selective to EO production[32,38].

Because of the great complexity of Ag surface structures under reaction conditions, theoretical studies in this field typically utilize bulk-truncated metal or oxide models to gain mechanistic insights[39–43] and for catalyst screening[44–46], while their efforts for revealing Ag phases largely rely on the knowledge from surface science experiments[47,48]. This is not least because first-principles methods are too computationally demanding to resolve the in situ surface structure even with advanced structure exploration methods[49]. Machine-learning atomistic simulations that emerged in recent years[50–56], however, could resolve the long-standing puzzles on ethene epoxidation on Ag catalysts[57–60]. As demonstrated by us recently, the machine learning-based automated search for optimal surface phases (ASOP) method, a grand canonical global optimization approach, can help to identify the surface phase on Ag surfaces under industrial reaction conditions[61].

In this Article, via theoretical prediction followed by catalysis experimental verification, we identify a thin Ag surface oxide phase as the active phase of ethene epoxidation, which is grown exclusively on Ag(100) under both $O_2$ and ethene high pressures at 500 K. This is achieved by exploring millions of likely surface oxide structures on major Ag facets and constructing the thermodynamics phase diagram. The identified phase, namely $O_5$ phase, features the unique subsurface oxygen surrounded by square-pyramidal $Ag_5$ coordination [$Ag_4OAg$], which is not present in surface oxides grown on other Ag surface facets ((111), (110)) and also not formed at low ethene or $O_2$ pressure. We provide theoretical evidence for $O_5$ phase and confirm its presence by fixed-bed catalytic tests and in situ infra-red (IR) spectroscopy characterization.

## Results

### Surface structures of Ag catalyst

To determine the relevant Ag phases under reaction conditions, we explore the potential energy surface (PES) of three major Ag facets, that is Ag(111), Ag(100) and Ag(110), under two sets of conditions, that is, the oxidation condition at 500 K and 1 bar of $O_2$, and the industrial reaction condition at 500 K and 1 bar of both ethene and $O_2$. The ASOP method (Methods and Supplementary Note 1) is used to solve the optimal $Ag_xO_y$(ethene)$_z$ phase for all six tasks (three surfaces at two conditions). In these ASOP simulations, the number of atoms and the supercell size are varied guided by a modified grand canonical Metropolis Monte Carlo scheme, which leads to the exploration of 176 distinct supercells and 11,395 distinct compositions. The ASOP method is based on stochastic surface walking global optimization using global neural network potential[62–64] (SSW-NN; Methods, Supplementary Tables 1 and 2, and Supplementary Figs. 1–3), as implemented in the large-scale atomic simulation with neural network potential (LASP) code developed by our group[65]. More than three million structure candidates have been explored by SSW–NN. The most stable surface phases at each composition and two conditions are collected and verified using density functional theory (DFT) calculations. All data are detailed in Supplementary Note 2 and Supplementary Figs. 4–7. We found that five tasks result in monolayer Ag surface oxides without ethene adsorption as the optimal phase, and only the task of Ag(100) under the industrial reaction condition results in a distinct phase featuring subsurface O and chemisorbed ethene.

Taking Ag(100) as the example, we show in Fig. 1a the surface energy contour map under the industrial reaction conditions, which is plotted using the most stable configuration at each $Ag_xO_y$(ethene)$_z$ composition ($Ag_xO_y$ surface oxide at a finite ethene coverage $z$). The colour represents surface energy (see equation (3) in Methods): the red zone corresponds to the structures with high surface energy, while the blue zone represents structures that are more energetically favourable.

With the most stable phase at each composition, we can plot the surface phase diagram on Ag(100) under various $O_2$ and ethene pressures, as depicted in Fig. 1b. It shows that as the $O_2$ pressure increases or temperature decreases, a transition from the metallic Ag(100) surfaces to several different surface oxide phases occurs, as depicted in Fig. 1c, illustrating the structure evolution with highlighting the atomic structure of the key phases. At low pressures (for example, <1 mbar) at 500 K, only the O adsorption phase (orange colour in Fig. 1b) and p(2√2 × √2) phase (yellow colour) are present, which were reported in surface science experiments (the inset of Fig. 1b, highlighting the typical surface science conditions)[48]. The atomic O atoms in these phases belong to $O_4\alpha$ and $O_4\beta$, respectively, highlighted in Fig. 1d. Notably, under typical conditions for catalytic reactions, the (100) surface turns out to be dominated by another two distinct phases, an $Ag_7O_5$ c(2√2 × 2√2) phase (green colour), namely, phase 100 in the region of lower pressure but higher temperature, and $O_5$ phase (blue colour) in the region of higher pressure but lower temperature. These two phases are close in surface energy—$O_5$ phase is 0.028 J m$^{-2}$ (0.014 eV per surface Ag) lower than the phase 100 at 500 K and 1 bar of both ethene and $O_2$ (hereafter referred to as the typical industrial condition). The phase diagram confirms the sensitivity of the surface structure to external conditions. We further elaborate the two critical phases in the following.

Phase 100 holds a (2√2 × 2√2) supercell of Ag(100) and has a surface energy of −0.364 J m$^{-2}$ (−0.189 eV per surface Ag), which was recently discovered by us[61]. All O species are tetra-coordinated and adsorbed on the surface as $O_4\alpha$ and $O_4\beta$ in Fig. 1d.

$O_5$ phase, represented by an $Ag_4O_3(C_2H_4)_1$ motif within the smallest p(√5 × 2) supercell (if ethene orientation is considered, the larger supercell with random ethene orientation is slightly more stable, for example, p(4 × 4) in Fig. 1c), is named for the presence of the unique square-pyramidal subsurface O ($O_5\beta$). This phase has 1.0 monolayer (ML) Ag and 0.75 ML O coverage. The surface energy is −0.392 J m$^{-2}$ (−0.203 eV per surface Ag, the same below), but if without adsorbed ethene, it will increase to −0.230 J m$^{-2}$ (−0.119 eV). As shown in Fig. 1c with a yellow background, this phase can be decomposed into three layer-by-layer structures, where the $O_5\beta$ atoms on the (100) facet (at the fourfold hollow site of Ag(100), that is [$Ag_4O$]) act as the first layer building block, which is then followed by the growth of an Ag–O network that resembles an $Ag_2O$(111) layer (Supplementary Fig. 5) with a nearly hexagonal Ag–O–Ag skeleton, and finally covered by ethene molecules chemisorbed on Ag atoms that locate at the six-member ring void of Ag–O–Ag skeleton and atop the $O_5\beta$ atom, that is, [$Ag_4OAg$]. We emphasize that the square-pyramidal subsurface O has not been reported previously, as O atoms generally prefer a tetrahedral or octahedral geometry, for example, in bulk $Ag_2O$ and on the surface oxides of Ag(111)[15,30,59].

Compared with Ag(100), Ag(111) and Ag(110) are much simpler in the phase diagram (Supplementary Figs. 6 and 7), which have the same most stable phase, under both oxidation and industrial reaction conditions. These two most stable phases on (111) and (110) facets are termed as phase 111 and phase 110, respectively. Therefore, under industrial reaction conditions, there are at least four coexisting phases on the Ag catalyst, that is, phase 111 on (111) facet, phase 110 on (110) facet, and phase 100 and $O_5$ phase on (100) facet. The population of these four phases can be estimated from the Wulff rule and Boltzmann distribution (Supplementary Note 1)—for instance, at 490 K and 1 bar of both ethene and oxygen, they are 0.31, 0.46, 0.02 and 0.21, respectively. The surface energies and atomic structures of phase 111 and phase 110 are briefly summarized as follows.

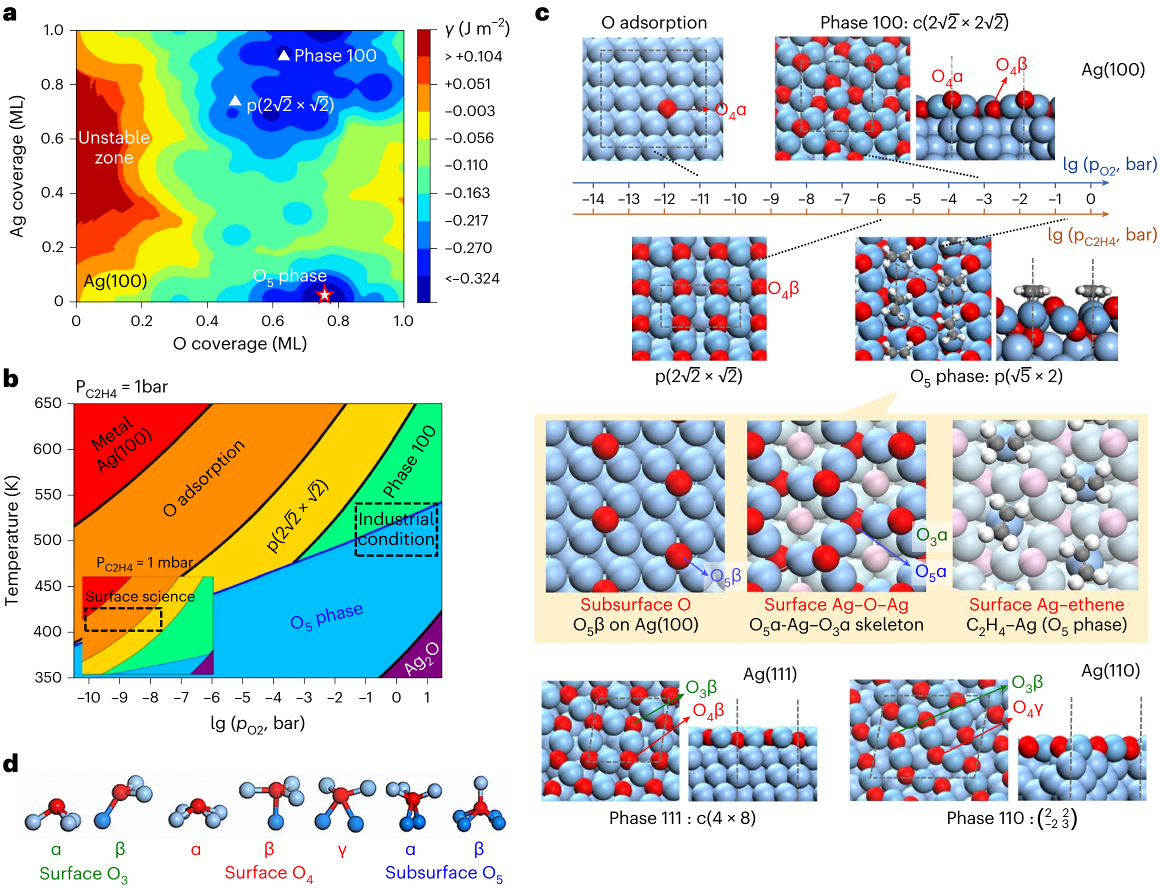

**Fig. 1 | Ag surface structure evolution under various conditions. a**, The potential energy surface contour map of (100) facet at 500 K and 1 bar of both oxygen and ethene from the ASOP simulation. Each point in this map represents an $Ag_xO_y(\text{ethene})_z$ ($z > 0$) composition, where the value of $z$ corresponds to the ethene coverage that yields the lowest surface energy. All the values of coverage are in monolayer (ML). **b**, The surface phase diagram on Ag(100) with the variation of oxygen pressure and temperature, in which ethene pressure is 1 bar for industrial condition (main figure) and 1 mbar for surface science condition (inset). **c**, The diagram of surface evolution on Ag(100) with the changes of gas pressures at 500 K, and the atomic structures of these phases (top and/or side views). The $O_5$ surface phase can be viewed as an assembly of three surface structures stacked layer-by-layer, as shown in the yellow background figures (stacking order from left to right). Listed structures (top and side) also include phase 111 and phase 110. **d**, Different types of oxygen species on Ag phases were revealed from ASOP simulations, categorized by the coordination number to surface Ag (blue) and subsurface Ag (deep blue). Colour code includes Ag, blue; C, grey; H, white; and O, red.

Phase 111 is the known c(4 × 8) reconstruction on Ag(111) and has a surface energy of −0.361 J m$^{-2}$ (−0.162 eV per surface Ag)[66]. All O species on the surface belong to either tri-coordinated ($O_3\beta$) or tetra-coordinated ($O_4\beta$) oxygen, as shown in Fig. 1d.

Phase 110 has the stoichiometry of $Ag_8O_8$ in an Ag(110) supercell with the lattice being $u = 2a + 2b$ and $v = -2a + 3b$ ($a$ = [001] and $b$ = [110]), consisting of 10 Ag atoms per layer. It has a surface energy of −0.471 J m$^{-2}$ (−0.344 eV per surface Ag). The O atoms on the surface are mostly $O_3\beta$ atoms, with a minority of $O_4\gamma$ atoms. Its structure features inter-connected zig-zag [Ag–O–Ag] chains (Fig. 1d), resembling the O-terminated $Ag_2O(110)$ surface.

## Electronic properties of the $O_5$ phase and surface oxides

Now we turn our attention to the differences between $O_5$ phase and the other surface oxides, which differ in the type of O species and the ethene adsorption ability. To this end, we first calculated the $O_{1s}$ binding energies of all four phases using DFT (Supplementary Table 4), which reveals that the anionic oxygen species in four phases are all in the range of 527–529 eV, consistent with previous XPS experimental findings and theoretical calculations[12,15,30]. The $O_{1s}$ binding energy of the $O_5\beta$ atom is in the middle (−528.1 eV).

We note that ethene can readily adsorb on $O_5$ phase with the calculated adsorption energy of −1.04 eV, which is far larger than its adsorption on the other surface oxides (approximately −0.4 eV). This is the key reason for the formation of $O_5$ phase under high pressures of both ethene and oxygen. Figure 2a further compares the projected density of states (p-DOS) peaks of the ethene carbon atoms and the Ag atom involved in adsorption before and after ethene adsorption. It shows that the $d$-band centre of the Ag atom shifts downward after ethene adsorption, confirming the covalent nature of Ag bonding with ethene. Consistently, a reduction in the intensity of ethene molecular orbitals also occurs after adsorption, including HOMO-1 ($1\pi_g$), HOMO ($2\pi_u$) and LUMO ($2\pi_g$), which suggests the π donation (from ethene to Ag) and back donation (from Ag to ethene) in the ethene–Ag bonding. In addition to π bondings, the HOMO-2 ($2\sigma_g$) orbital of ethene (peak [1] in Fig. 2a) splits into two peaks after adsorption with the major bonding state (at −6.5 eV) indicated by peak [2] in Fig. 2a. The wave function of the state tells that the $2\sigma_g$ of ethene interacts with $d_{z^2}$ of Ag atom, which is activated by the $p_z$ orbital of the underlying $O_5\beta$. Moreover, the $2\sigma_g$ of ethene mixes with the $p$ orbital of the surface $O_3$ atoms, delocalizing to the whole [Ag–O–Ag] oxide network. The electronic structure results confirm the critical role of subsurface $O_5\beta$ in promoting ethene adsorption, which was long suspected in literatures[67,68].

The strong ethene chemisorption behaviour at $O_5$ phase thus motivated us to explore any measurable quantities for experimental characterization. Figure 2b compares the simulated IR spectra of the

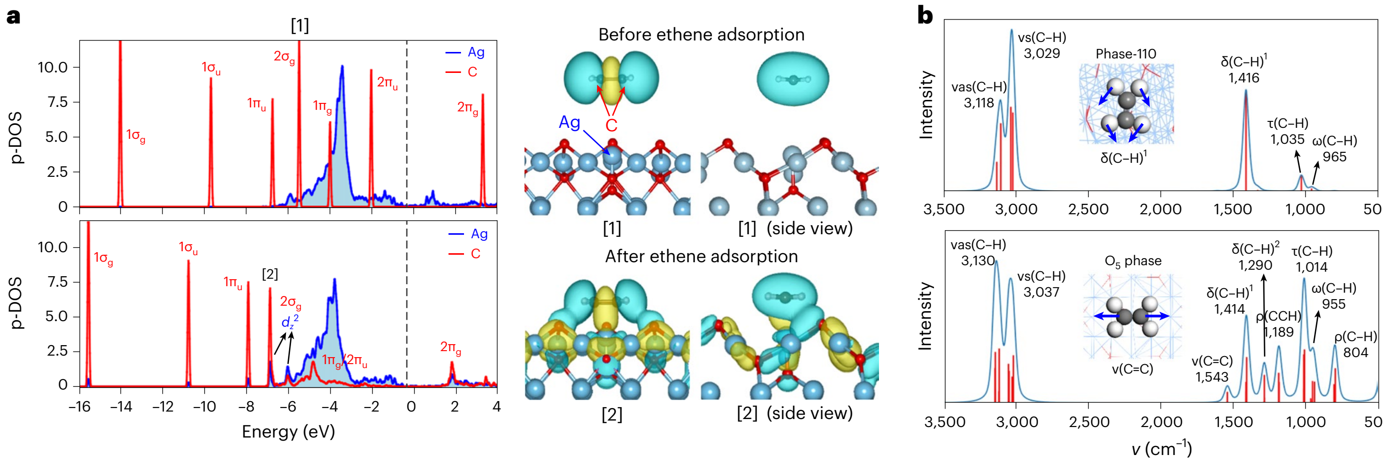

**Fig. 2 | Electronic properties and vibrational spectrum of Ag surface oxides.** **a**, The p-DOS of carbon species (red line) and Ag atom below ethene molecule (blue line) on $O_5$ phase before (peak [1] referred, ethene is 5 Å above the anchored Ag atom) and after (peak [2] referred) ethene adsorption, in which the dashed line represents the Fermi level. The inset plots the wave functions (negative in blue and positive in yellow, isosurface value of $2.5 \times 10^{-4}$ Bohr$^{-3/2}$) of the $2\sigma_g$ related states, labelled in the p-DOS plot as the peak [1] and [2]. **b**, The simulated vibrational IR spectra of adsorbed ethene on phase 110 and $O_5$ phase. The colour code is as in Fig. 1.

adsorbed ethene on phase 110 and $O_5$ phase. For phase 110, the IR active modes correspond to C–H stretching (ν(C–H) at above 3,000 cm$^{-1}$), an asymmetric type of C–H scissoring (δ(C–H)$^1$ at 1,416 cm$^{-1}$), and the longitudinal bending modes of C–H at about 1,000 cm$^{-1}$, being the same as ethene in the gas phase. However, on $O_5$ phase, many more bands are infra-red active. These include the stretching vibration of the C=C bond (ν(C=C)) at 1,543 cm$^{-1}$, a symmetric type of C–H scissoring (δ(C–H)$^2$ at 1,290 cm$^{-1}$), and the rocking modes at 1,189 and 804 cm$^{-1}$. Importantly, the ν(C=C) peak is well known to be IR inactive at 1,640 cm$^{-1}$ for ethene gas, which becomes IR active after adsorption, redshifting to 1,543 cm$^{-1}$. This phenomenon can be attributed to the asymmetric Ag–O–Ag chemical environment for the adsorbed ethene interacting with $O_5$ phase. This observation offers a key clue to verify the presence of $O_5$ phase in experiments.

## Reaction behaviours and overall mechanism

After having determined all phases relevant to industrial conditions, we then explore the reaction pathways on each phase using the automated SSW reaction sampling method based on G-NN potential[38,69]. The lowest energy pathways on the monolayer surface oxides, including phase 111, phase 100 and phase 110, are detailed in Supplementary Figs. 8–10, revealing that ethene prefers the full oxidation pathway (to $CO_2$) on these surfaces with phase 110 exhibiting the highest activity. Importantly, only $O_5$ phase is found to be selective towards EO, and the lowest energy pathway is elaborated in the following.

The DFT-based free energy reaction profile on $O_5$ phase is shown in Fig. 3a, together with the snapshots of key reaction intermediates shown in Fig. 3b. This lowest energy pathway corresponds to the ethene coverage of 0.125 ML (for surface Ag atoms) with half occupation of $O_5$β sites (Supplementary Note 3). Initially, ethene adsorbs on the Ag–$O_5$β site with the free energy gain by 0.31 eV. Subsequently, the adsorbed ethene combines with a nearby surface $O_3$ to form oxametallacycle (OMC) intermediate[7,70–72], with a barrier of 0.86 eV. Similar to the reaction channels found on metallic Ag surfaces, three potential OMC conversion routes occur via three distinct transition states (TSs), that is, the cyclization to EO, the H-transfer to acetaldehyde (AA), and the dehydrogenation to 2-oxoethyl (OE). Notably, the EO production route possesses the lowest barrier, with its transition state (TS2-EO) being 0.12 eV and 0.14 eV lower in free energy than TS2-OE and TS2-AA, respectively. In TS2-EO, the two [C–O] bonds are not identical in length, being 1.43 Å and 1.85 Å. Finally, the EO molecule, which is only weakly adsorbed on the surface, desorbs into the gas phase (free energy decreases by 0.09 eV).

For the other surfaces, the initial reaction steps are the same, and the major difference lies in the selectivity towards different products, as measured by the height of TS2. Take phase 110, the most active phase for $CO_2$ production, as an example, where the OMC dehydrogenation route exhibits the lowest barrier, which is 0.56 eV lower than that of the cyclization channel (see the inset table of Fig. 3a).

Once EO/$CO_2$ products are formed, the Ag surface is left with O vacancies. The possible pathways for the healing of O vacancies are also explored on these phases (Supplementary Figs. 11–16). For example, the $O_2$ activation on $O_5$ phase with O vacancies is found to be kinetically difficult, with a barrier of 1.64 eV for $O_2$ dissociation and 1.49 eV for the bimolecular reaction ($CH_2CH_2 + O_2$) to form $CH_2CH_2OO$, which is much higher than that of surface O diffusion (0.62 eV barrier). This suggests that $O_5$ phase alone cannot complete the catalytic cycle of ethene epoxidation. However, $O_2$ dissociation on the other phases is facile, for example, the barrier of $O_2$ dissociation with two O vacancies is 0.27 eV and 0.66 eV on phase 111 and phase 110, respectively. Considering that the O diffusion on all these surfaces is low in barrier (<0.78 eV), and phase 111 and phase 110 are another two major phases under reaction conditions, the healing of O vacancies on $O_5$ phase can be accomplished through the diffusion of O atoms[73], for example, from neighbouring phase 111 and phase 110 surfaces. A full microkinetics analysis of all DFT-calculated ethene epoxidation pathways is performed to compare with experimental data in the following section.

We have also examined the stretching frequency of $O_2$ (ν(O–O)) adsorbed at an O vacancy on phase 111, phase 110, phase 100 and $O_5$ phase, which are 815, 876, 751 and 744 cm$^{-1}$, respectively (Supplementary Figs. 12 and 14–16). The wave numbers agree with the in situ Raman spectrum for chemisorbed O–O species, falling within the range of ~750–950 cm$^{-1}$ (refs. 74–76), indicating the catalyst under reaction conditions should not be a single phase and there is no clear Raman evidence on the presence of $O_5$ phase in literature.

## Catalytic ethene epoxidation experiments

To verify the theoretical predictions on the active phase and the reaction kinetics, we then conducted a series of catalytic experiments in the fixed-bed reactor with fine-tuned reaction conditions. A standard impregnation approach is used to synthesize the Ag/α-$Al_2O_3$ catalyst (Methods). The X-ray diffraction characterization (Supplementary Figs. 17 and 18) of the as-synthesized catalyst confirms the metallic nature of the Ag phase (no detectable $Ag_2O$ peak). The transmission electron microscope (TEM) image in Fig. 4a further reveals the spherical

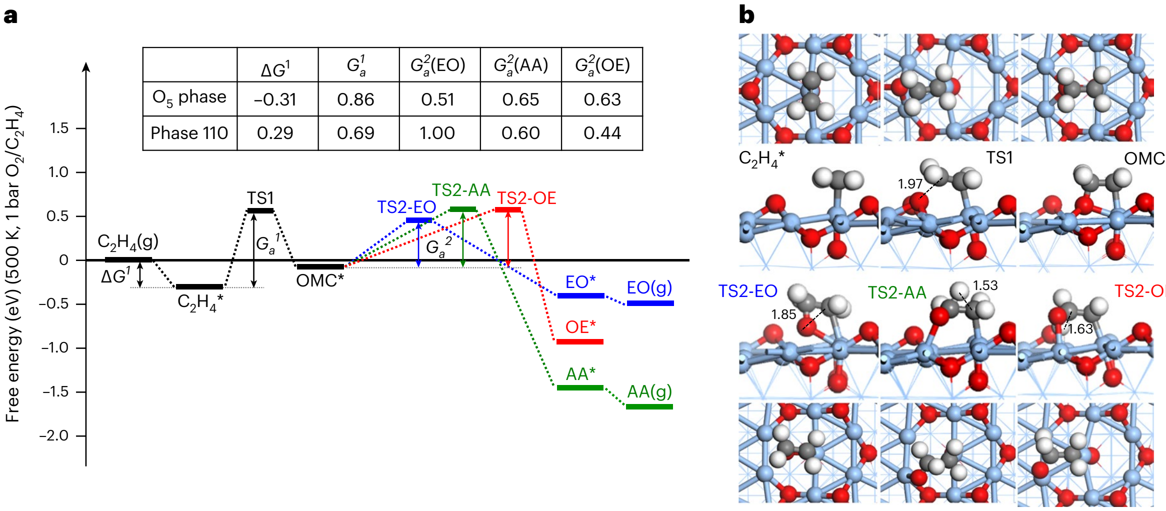

|  | $\Delta G^1$ | $G_a^1$ | $G_a^2$(EO) | $G_a^2$(AA) | $G_a^2$(OE) |
|---|---|---|---|---|---|
| $O_5$ phase | −0.31 | 0.86 | 0.51 | 0.65 | 0.63 |
| Phase 110 | 0.29 | 0.69 | 1.00 | 0.60 | 0.44 |

**Fig. 3 | Gibbs free energy profile and overall mechanism.** **a**, The calculated Gibbs free energy profile of ethene epoxidation on $O_5$ phase. The elementary barrier and reaction energy (in eV) on $O_5$ phase and phase 110 are listed in the inset table. Asterisk indicates adsorbate. **b**, The reaction snapshots along the pathways on $O_5$ phase, with key bond length (Å) labelled. The colour code is as in Fig. 1.

shape of large Ag nanoparticles, which are supported on α-$Al_2O_3$ at a mean particle size of 82 ± 40 nm (standard deviation, the same below). The (200) Ag plane together with the characteristic α-$Al_2O_3$ (110) are visible from the high-resolution TEM image in Fig. 4b. The catalytic performance of the synthesized catalyst is collected at a steady state after 1 h of continuous operation. Fig. 4c further demonstrates the good stability of the catalyst in terms of selectivity and conversion performance after more than 200 h of reaction. The catalyst attains a 59.4 ± 1.2% EO selectivity at a controlled low ethene conversion (1%), exhibiting a slightly elevated selectivity with lower conversion compared with the previously reported experimental data (30–50% selectivity at conversion less than 5%)[4].

Through systematic variations in reaction temperature and $O_2$ pressure, we investigate the dependence of EO selectivity on the reaction conditions, as shown in Fig. 4d,e. The EO selectivity is very sensitive to the reaction temperature and achieves the highest value 61.7 ± 0.5% at 490 K. A change of 50 K in temperature will rapidly reduce the selectivity to ~40%. On the other hand, the EO selectivity is less sensitive to the $O_2$ pressure, which gradually escalates from 55.8 ± 0.4% to 62.0 ± 0.1% with the increase of $O_2$ pressure from 0.1 to 2.5 bar (Fig. 4e).

Since adsorbed ethene is predicted to exhibit a characteristic C=C stretching mode (Fig. 2b), we carried out in situ Fourier transform IR (FT-IR) spectroscopy and gas chromatography mass spectrometry (GC–MS) to analyse the reaction intermediates and products of ethene epoxidation above 420 K. The existence of both $CO_2$ and EO in the products is first confirmed by the GC–MS analysis (Supplementary Fig. 19) above 460 K. Figure 4f displays a sequence of FT-IR spectra of the catalyst under 0.1 bar of both $C_2H_4$ and $O_2$ with the increase of temperature, where the background spectra collected at each temperature were subtracted (negative/positive peaks, thus indicating the products/the consumed reactants). At temperatures above 500 K, the FT-IR exhibits prominent negative peaks at 2,362 and 2,332 $cm^{-1}$, which are the symmetric stretching peaks ($\nu_{as}$(OCO)) of $CO_2$. In addition, the negative peaks at 948, 1,338, 1,400, 1,443 and 1,583 $cm^{-1}$ are also observed in FT-IR above 460 K, which can be attributed to C–H longitudinal bending of 948 $cm^{-1}$, two types of C–H scissoring for 1,338–1,443 $cm^{-1}$ and C=C stretching vibration of 1,583 $cm^{-1}$ (Fig. 2b), respectively. We note that the 1,583 $cm^{-1}$ peak emerges only when both $C_2H_4$ and $O_2$ are present under reaction conditions, in companion with the appearance of the $CO_2$ peak (also see Supplementary Figs. 20 and 21 for time-resolved IR spectra at 500 K). The identification of 1,583 $cm^{-1}$ peak confirms the theoretical prediction of the IR-active C=C stretching vibration (ν(C=C)) for adsorbed ethene on $O_5$ phase.

Apart from in situ IR experiment that confirms the presence of adsorbed ethene, we also conducted in situ isotope ($^{18}O$) Raman characterization for the Ag/α-$Al_2O_3$ catalyst under the same condition (0.1 bar of $C_2H_4$ and $O_2$). As shown in Supplementary Fig. 22a, there are peaks of around 330 $cm^{-1}$, 610 $cm^{-1}$ and ~750–900 $cm^{-1}$ depending on temperatures, in which the peak at 771 $cm^{-1}$ emerges only after the temperature rises to above 393 K. Supplementary Fig. 22b further indicates that this peak (771 $cm^{-1}$) disappears during $H_2$ reduction, but can be retrieved only in a mixed reactant gas ($C_2H_4 + O_2$), characterizing a phase formed only under the reaction conditions. In the subsequent isotope experiment of $^{18}O_2$, we reveal the red shift of peaks from 887, 771, 333 $cm^{-1}$ to 870, 739, 305 $cm^{-1}$ (Supplementary Fig. 22c), and the formation of $E^{18}O$ ($CH^{18}O$, *m*/*z* of 31) and $C^{18}O_2$ (*m*/*z* of 48) in the online mass spectrum are also detected (Supplementary Fig. 22d). From our DFT calculations, the calculated O–O vibrational frequencies of adsorbed $O_2$ on $O_5$ phase and phase 110 are 744 $cm^{-1}$ and 876 $cm^{-1}$, which red shift to 702 $cm^{-1}$ and 826 $cm^{-1}$ with $^{18}O_2$ isotope, respectively. This suggests that the experimental phase at 771 $cm^{-1}$ ($^{16}O$) and 739 $cm^{-1}$ ($^{18}O$ isotope) could correspond to the $O_2$ adsorption on the $O_5$ phase that forms under reaction conditions and relates closely with the mixed gas condition.

## Microkinetics simulation

Based on the DFT reaction profiles on all major phases, we performed the microkinetics simulation to rationalize the experimental kinetics results. Compared with previous kinetic models[40,77,78], our model considers the coexistence of all surface phases on the main Ag facets under reaction conditions. In total, 42 elementary steps on the relevant phases and 42 distinct species are considered in the microkinetics model. All the ordinary differential equations are solved by the backward differentiation formula method[79], the solution of which is further polished by Newton's method optimization[80]. These are implemented in our recently developed microkinetics-guided machine-learning pathway search package[55]. All the kinetic data of our model are listed in Supplementary Table 7 together with the detailed analysis on the degree of rate/selectivity control, apparent activation energy, reaction orders and the comparison of turnover frequency (TOF) between theory and experiment (Supplementary Tables 8 and 9 and Supplementary Figs. 25–26).

Our microkinetics results are shown in the dashed lines of Fig. 4d,e to compare with the experimental kinetics data. As depicted in the

https://doi.org/10.1038/s41929-024-01135-2

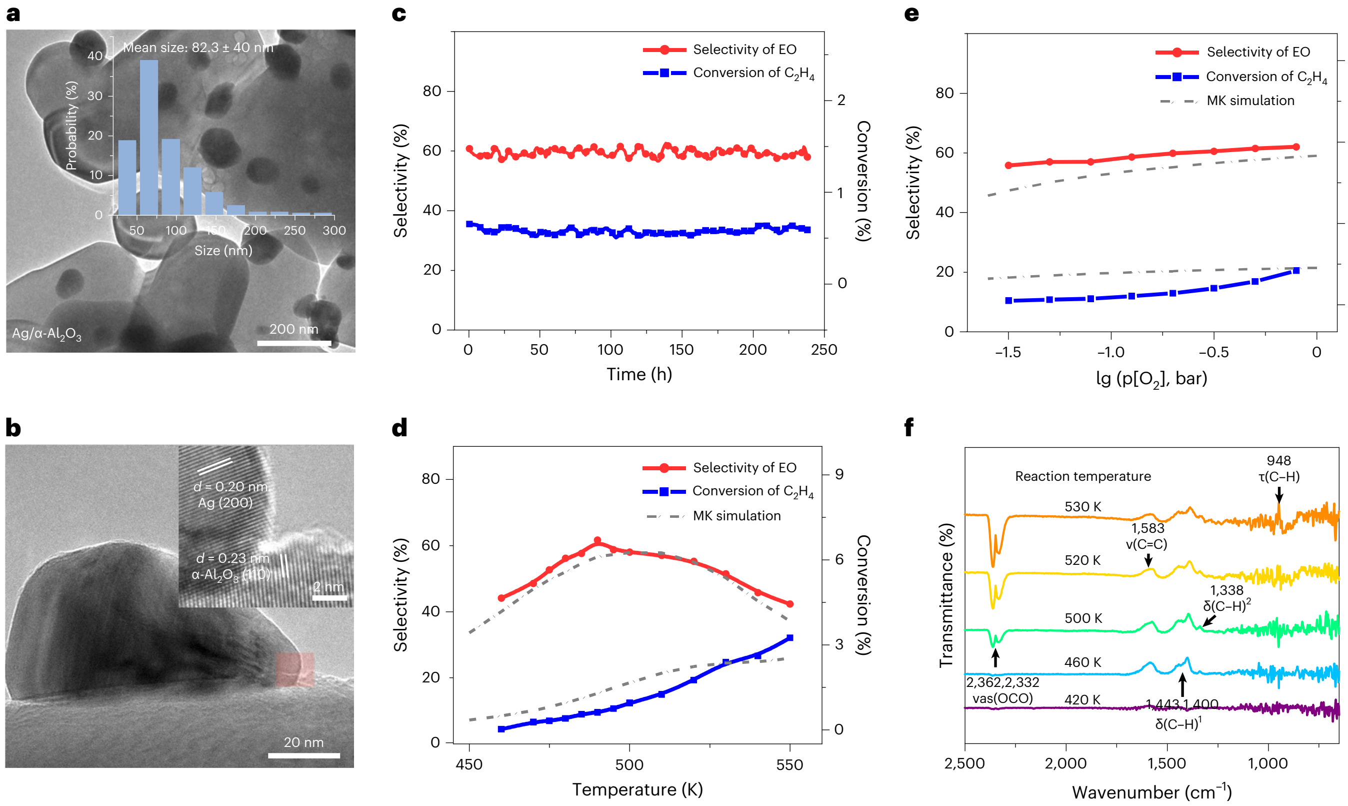

**Fig. 4 | Structure characterizations and catalytic performance of Ag/α-Al$_2$O$_3$.** **a**, TEM images and corresponding size distributions of Ag/α-Al$_2$O$_3$. **b**, High-resolution TEM image of Ag/α-Al$_2$O$_3$. The inset is the magnified image of the rectangular region. **c**, Dependence of C$_2$H$_4$ conversion and EO selectivity on time-on-stream for Ag/α-Al$_2$O$_3$ at reaction conditions of 490 K, 1 bar C$_2$H$_4$, 1 bar O$_2$ and gas hourly space velocity of 120,000 ml g$_{Ag}^{-1}$ h$^{-1}$. **d**, Relationship between the C$_2$H$_4$-conversion/EO-selectivity and reaction temperature under 1 bar C$_2$H$_4$ and 1 bar O$_2$ pressure of Ag/α-Al$_2$O$_3$ and the simulated results from the microkinetics (MK) model. **e**, EO selectivity and C$_2$H$_4$ conversion with increasing O$_2$ pressure at reaction conditions of 490 K, 1 bar C$_2$H$_4$ and the simulated results from the microkinetics model. The range and standard deviation of all the measured selectivity and conversion data are detailed in Supplementary Table 6. **f**, In situ FT-IR spectra as a function of temperature under 0.1 bar C$_2$H$_4$ and 0.1 bar O$_2$ pressure for Ag/α-Al$_2$O$_3$.

**Table 1 | Reaction rates from microkinetic simulation**

| Phases | Phase 111 | Phase 110 | Phase 100 | O$_5$ phase |
|---|---|---|---|---|
| Facet | (111) | (110) | (100) | (100) |
| Population | 0.31 | 0.46 | 0.02 | 0.21 |
| $r$(EO) | 3.7 | 0.0 | 0.1 | 839.7 |
| $r$(CO$_2$) | 164.0 | 1,010.3 | 7.0 | 109.7 |

The microkinetics formation rates to EO and CO$_2$ (molecule s$^{-1}$) for the four major phases under reaction conditions. The Ag surface facets on which these four phases grow and the populations of them are also listed. The reaction condition is at 490 K with C$_2$H$_4$ and O$_2$ pressures at both 1 bar.

figures, a good agreement on the trend of kinetics is achieved, which indicates the mechanism and kinetics results from DFT can well capture the impact of temperature and O$_2$ pressure on selectivity. By analysing the kinetics results, we found that the phase 110 and O$_5$ phase are critical to the overall selectivity—the former favouring CO$_2$ production and the latter leading to EO products, as reflected by Table 1, where the phase populations and the EO and CO$_2$ formation rates for all four phases under the reaction conditions are listed.

From Table 1, we can conclude that it is the population of phase 110 and O$_5$ phase grown on (110) and (100) surface facets, respectively, govern largely the EO selectivity. In particular, the population of O$_5$ phase ($w_{O5}$) is influenced by temperature and the pressure of C$_2$H$_4$ and O$_2$, since it can transform to the non-selective phase 100. Conversely, the population of phase 110 ($w_{110}$) can be treated as a constant under reaction conditions, since it is the only dominant phase on the (110) facet that forms at as low as 10$^{-8}$ bar of O$_2$ pressure ($p_{O2}$), and the morphology of Ag catalyst (large nanoparticle) is little affected by the subtle changes of the reaction conditions. With these understandings, a simplified kinetics model for computing selectivity $S$ is then derived as shown in equation (1).

$$S = \frac{w_{O5}(P_{C2H4},P_{O2},T)r_{O5}(T)}{w_{110}r_{110}(P_{C2H4},T)+w_{O5}(P_{C2H4},P_{O2},T)r_{O5}(T)}$$
$$\frac{1}{S} - 1 = \frac{w_{110}}{w_{O5}(P_{C2H4},P_{O2},T)\times\frac{r_{O5}(T)}{r_{110}(P_{C2H4},T)}} \qquad (1)$$

where $w$ represents the phase population, $r_{O5}$ is the rate to produce EO, controlled by the surface reaction of ethene, and $r_{110}$ is the reaction rate to produce CO$_2$, which is related to both ethene adsorption step and subsequent surface reactions (Fig. 3a). The equation (1) can be further derived (Supplementary Note 5) to

$$\frac{1}{S} - 1 = e^{(\alpha_1+\beta_1 T^{-1})}p_{O2}^{-0.5} + e^{(\alpha_2+\beta_2 T^{-1})} \qquad (2)$$

where $\alpha_1$, $\beta_1$, $\alpha_2$ and $\beta_2$ are four parameters determined by the kinetics data—$\alpha_2$ and $\beta_2$ relating to the free energy barriers of EO and CO$_2$ formation on phase 110 and O$_5$ phase, while $\alpha_1$ and $\beta_1$ further include surface free energy difference between phase 100 and O$_5$ phase. By fitting to our microkinetics results, we have calculated the value of $\alpha_1$, $\beta_1$, $\alpha_2$ and $\beta_2$ to be 18, −9.7 × 10$^3$, −14 and 6.8 × 10$^3$, respectively, which follows the same trend as the value fitted to experimental data, that is, 30, −1.6 × $10^4$, −8.3 and 3.9 × $10^3$.

Equation (2) provides a straightforward way to understand the epoxidation kinetics. The volcano-type curve of the selectivity-temperature curve in Fig. 4d is due to the negative value of $\beta_1\beta_2$ (<0), caused by the opposite response of $w_{O5}$ and $r_{O5}/r_{110}$ to temperature (the high temperature hinders ethene adsorption, thus lowering $w_{O5}$ but increasing $r_{O5}/r_{110}$, also see Supplementary Note 5). Moreover, the monotonous selectivity–$p_{O2}$ relation in Fig. 4e is due to $S \propto p_{O2}^{0.5}$, as $p_{O2}$ affects positively $w_{O5}$ by increasing $O_5$ phase population (see phase diagram in Fig. 1).

The active phase structure revealed here facilitates us to understand why silver is not applicable for longer alkene epoxidation. Our calculations show that propene oxidation on $O_5$ phase, as depicted in Supplementary Fig. 32, favours the dehydrogenation of the terminal $CH_3$ group, the so-called allylic hydrogen stripping route[81]. This leads to the generation of a stable allyl radical ($CH_2CHCH_2$), which subsequently undergoes full oxidation. The OMC ($CH_3CHCH_2O$) intermediate to epoxide is energetically unfavourable by 0.34 eV compared with the allylic hydrogen stripping route. Apparently, this is because while the C=C bond of propene is activated on $O_5$ phase, the additional methyl group of propene can also interact favourably with the active surface $O_3$ atom, facilitating C−H breaking in the methyl group and finally leading to deep oxidation. This observation suggests that a universal epoxidation catalyst should be able to both activate the C=C bond and eliminate any possible C−H activation sites. The finding of materials/dopants to enhance the formation of subsurface O and reduce the activity of surface O species should be the direction for designing better alkene epoxidation catalysts.

## Conclusions

In summary, through the large-scale grand canonical global structure exploration using G-NN potentials, we uncover a critical surface oxide phase, $O_5$ phase, from more than three million structure candidates. This phase grows on Ag(100) and exhibits both square-pyramidal subsurface O and strongly adsorbed ethene with special electronic properties under industrial conditions (for example, 1 bar of both $O_2$ and $C_2H_4$ at ~500 K), but is not favoured thermodynamically under surface science low-pressure conditions when Ag catalyst fails to produce EO with high selectivity. With the structures and the reaction pathways fully explored on all major Ag facets, we show that $O_5$ phase is the only phase selectively producing EO, in which the EO formation barrier is 0.12 eV lower than that of the combustion routes, while the other surface oxide phases lead to mainly ethene combustion. Importantly, $O_5$ phase has a low activity towards $O_2$ dissociation and the O supply of $O_5$ phase requires the cooperation of the inter-phase and/or inter-termination sites. Guided by theory, our catalysis experiments of home-made Ag/α-$Al_2O_3$ catalyst achieve a long-term (>200 h) high EO selectivity (59.4 ± 1.2%) at 490 K and 1 bar of both $O_2$ and $C_2H_4$. Importantly, the existence of adsorbed ethene on $O_5$ phase is verified by FT-IR, showing the IR-active C=C stretching vibration at 1,583 $cm^{-1}$, which is the precursor for ethene oxidation. The measured kinetics in temperature–selectivity and $O_2$ pressure–selectivity relationships agree with the microkinetics simulation and a simplified kinetics model only including $O_5$ phase (constituting ~21% surface area of the Ag catalyst) and the non-selective (110) phase (~47% area of catalyst) is derived to explain the observed ethene epoxidation kinetics on the Ag catalyst. This work provides a state-of-the-art solution to reveal the complex, dynamic catalyst evolution under industrial conditions, which could benefit greatly the catalyst design at the atomic level.

## Methods

### Machine-learning atomic simulation

All the atomic simulations using the SSW method[62] for PES sampling based on G-NN potentials[63,64] were carried out using the LASP package (www.lasphub.com)[65]. The final dataset for the Ag–C–H–O four-element G-NN potential used in this study consists of 62,912 configurations calculated using highly accurate DFT. Each elementary neural network utilizes 305 power-type structural descriptors to predict atomic energies. The network architecture comprises three hidden layers (305-80-50-50-1), with a total of 124,524 learnable parameters. To depict the complex atomic environment in catalysis, the cut-off radius in G-NN potential is set from 1.00 Å to 7.20 Å, and the power ($n$) used in power-type structural descriptors is up to 16. The hyperbolic tangent function is utilized as the activation function in all the hidden layers. The G-NN potential is in ASCII (text) format and all parameters are human-readable (accessible from the download link provided). The root mean-square errors for energy and force are 5.381 meV per atom and 0.090 eV $Å^{-1}$, respectively. Further details on the SSW–NN method, G-NN training and G-NN benchmarking against DFT can be found in Supplementary Methods.

### The ASOP algorithm

The ASOP algorithm[61] is utilized to determine the optimal surface phases under a wide range of possible compositions ($Ag_xO_y(C_2H_4)_z$ on various surface periodicities) in a parallel sampling manner. For completeness, here we briefly outline the algorithm of this method. The ASOP simulation is a parallel composition space exploration method. The composition space is discretized into a series of grids, each representing a possible surface periodicity. These grids contain numerous grid points, where each point corresponds to a specific composition (for example, $Ag_3O_2(C_2H_4)_1$). The simulation begins with the coarsest grid (the smallest cell), focusing on compositions with the lowest costs to efficiently sample favourable configurations. Knowledge is then propagated from grid to grid, directing computational efforts towards potentially favourable compositions in finer grids. This process continues until all designated grids have been thoroughly explored.

For every composition, an initial structure is randomly generated. The SSW–NN method is used for global optimization of the PES, yielding the most stable configuration. This configuration is subsequently subjected to thermodynamics analysis. This analysis evaluates composition preferences, that is, the surface free energy, as defined by equation (3).

$$\gamma = \frac{E_{\text{total}} - E_{\text{slab}} - N_{\text{Ag}}\mu_{\text{Ag}} - N_{\text{O}}\mu_{\text{O}} - N_{\text{C2H4}}(\mu_{\text{C2H4}} - G_{\text{C2H4,ads}})}{A} \tag{3}$$

In this equation, $E_{\text{total}}$ and $E_{\text{slab}}$ are the energy of the total structure and the Ag slabs, respectively. $N$ and $\mu$ are the number and chemical potential of a given species, respectively (see Supplementary Note 1 for the estimation of $\mu$). $A$ is the surface area. $G_{\text{C2H4,ads}}$ represents the thermal effects of the adsorbed ethene, including the adsorbate entropies and enthalpies.

### DFT calculations

All low-energy structures and key intermediates along the reaction profile were verified using DFT calculations, which were conducted using the plane-wave VASP package[82]. The electron–ion interaction was represented using the projector-augmented wave pseudopotential[83], and the exchange functional was evaluated with generalized gradient approximation of Perdew–Burke–Ernzerhof[84]. A kinetic energy cut-off of 450 eV was used, and the convergence criteria for energy and force were set to $10^{-6}$ eV and 0.05 eV $Å^{-1}$, respectively. The Monkhorst–Pack k-mesh was chosen to be 30 times the reciprocal lattice vectors (1/30 $Å^{-1}$). For all calculations, including those involving the G-NN potential, the van der Waals correction was accounted for using the DFT-D3 method with zero damping[85]. This correction is crucial for accurately describing the interactions between Ag and O[10], as well as molecular adsorption.

To construct the free energy profile, we incorporated zero-point energy and free energy corrections of gaseous species and adsorbates into all kinetic data, which were estimated from standard thermodynamics equations[86]. Various computational methods were also used and compared (Supplementary Table 5) to ensure the accuracy of the kinetic data. It's important to note that except for the PES contour map in Fig. 1a, all data presented in this study are from DFT calculations, allowing for precise comparisons between our theoretical predictions and experimental results.

The ΔSCF method was used to estimate the $O_{1s}$ binding energy. This method calculates the energy difference between the ground state and a state in which a core hole is introduced[15]. The calculated value is then adjusted to account for the experimental XPS $O_{1s}$ signal of bulk $Ag_2O$, which is 529.2 eV (ref. 87).

### Surface models

For the Ag surface structure models, we utilized six slab layers for Ag(110) and four slab layers for both Ag(111) and Ag(100). In these models, the bottom two layers were kept fixed. Except for phase 110, supercell models were used for free energy profile calculations to better isolate the reactant from itself in nearby cells. Specifically, a (4 × 4) supercell of Ag(111) was used for phase 111, and a (4 × 4) supercell of Ag(100) was used for phase 100 and $O_5$ phase. All the surface structures of these four phases and their transition states in ethene epoxidation reaction pathways are provided in Supplementary Data 1 in VASP POSCAR format.

### Synthesis of $Ag/\alpha\text{-}Al_2O_3$ catalysts

The $\alpha\text{-}Al_2O_3$ required high-temperature calcination at 1,800 K for 2 h in a muffle furnace to decrease its specific surface area. By following the procedure reported in the literature[88], $Ag/\alpha\text{-}Al_2O_3$ was synthesized using silver oxalate ($Ag_2C_2O_4$) as the silver precursor. The $Ag_2C_2O_4$ was obtained by dissolving 10 g of oxalic acid ($H_2C_2O_4$) and 1 g of $AgNO_3$ in 100 ml of deionized water, followed by stirring for 1 h. Subsequently, 1.0 g of $Ag_2C_2O_4$ was mixed with 0.89 ml of $H_2O$ and 0.89 ml of ethenediamine ($C_2H_8N_2$) solution. The resulting mixture was then impregnated onto 3.2 g of $\alpha\text{-}Al_2O_3$, freeze-dried in vacuum and calcined at 300 °C in air for 4 h. The resulting $Ag/\alpha\text{-}Al_2O_3$ catalyst had an approximate Ag loading of 18.2% by weight.

### Catalytic testing

All catalytic reactions were performed in a continuous flow fixed-bed microreactor. For comparison, all samples contain 50 mg Ag, mixed with 15 g quartz sand. Before the reaction, the catalysts were pre-treated in pure $O_2$ at 300 °C for 2 h, and then cooled to the reaction temperature. The products were analysed by an online GC–MS (Agilent 8860-5977B) with HP-PLOT Q capillary column. The activity and selectivity of the catalysts were taken from the steady data that is after 1 h in the stream. The ethene conversion and ethene oxide selectivity ($S_{EO}$) were calculated by using equations (4) and (5), respectively,

$$\text{Conv} = \frac{1/2\text{CO}_{2(\text{out})} + \text{EO}_{(\text{out})}}{1/2\text{CO}_{2(\text{out})} + \text{EO}_{(\text{out})} + \text{C}_2\text{H}_{4(\text{out})}} \times 100\% \quad (4)$$

$$S_{\text{EO}} = \left(\frac{\text{EO}_{(\text{out})}}{1/2\text{CO}_{2(\text{out})} + \text{EO}_{(\text{out})}}\right) \times 100\% \quad (5)$$

where in/out subscripts refer to the concentration measured in the inlet/outlet port.

## Data availability

All data generated or analysed during this study are included in this published article (and its supplementary information files). Data are also available from the corresponding author upon request.

## Code availability

The software code for LASP and the NN potentials used within the article are available from the corresponding author upon request or on the website: LASP software, http://www.lasphub.com; the LASP binary code for the Ag–C–H–O system, http://www.lasphub.com/supportings/lasp-free.tgz, and Ag–C–H–O G-NN potential, http://www.lasphub.com/supportings/AgCHO.pot.

## References

1. Rebsdat, S. & Mayer, D. *Ullmann's Encyclopedia of Industrial Chemistry*, 547–572 (American Cancer Society, 2001).
2. Serafin, J. G., Liu, A. C. & Seyedmonir, S. R. Surface science and the silver-catalyzed epoxidation of ethylene: an industrial perspective. *J. Mol. Catal. A* **131**, 157–168 (1998).
3. Lambert, R. M., Williams, F. J., Cropley, R. L. & Palermo, A. Heterogeneous alkene epoxidation: past, present and future. *J. Mol. Catal. A* **228**, 27–33 (2005).
4. Pu, T., Tian, H., Ford, M. E., Rangarajan, S. & Wachs, I. E. Overview of selective oxidation of ethylene to ethylene oxide by Ag catalysts. *ACS Catal.* **9**, 10727–10750 (2019).
5. Kilty, P. A. & Sachtler, W. M. H. The mechanism of the selective oxidation of ethylene to ethylene oxide. *Catal. Rev.* **10**, 1–16 (1974).
6. Cant, N. W. & Hall, W. K. Catalytic oxidation: VI. Oxidation of labeled olefins over silver. *J. Catal.* **52**, 81–94 (1978).
7. Linic, S. & Barteau, M. A. Formation of a stable surface oxametallacycle that produces ethylene oxide. *J. Am. Chem. Soc.* **124**, 310–317 (2002).
8. Ozbek, M. O. & van Santen, R. A. The mechanism of ethylene epoxidation catalysis. *Catal. Lett.* **143**, 131–141 (2013).
9. Michaelides, A., Reuter, K. & Scheffler, M. When seeing is not believing: oxygen on Ag(111), a simple adsorption system? *J. Vac. Sci. Technol. A* **23**, 1487–1497 (2005).
10. Schmid, M. et al. Structure of Ag(111)-p(4x4)-O: no silver oxide. *Phys. Rev. Lett.* **96**, 146102 (2006).
11. Schnadt, J. et al. Revisiting the structure of the p(4x4) surface oxide on Ag(111). *Phys. Rev. Lett.* **96**, 146101 (2006).
12. Martin, N. M. et al. High-coverage oxygen-induced surface structures on Ag(111). *J. Phys. Chem. C.* **118**, 15324–15331 (2014).
13. Derouin, J., Farber, R. G., Turano, M. E., Iski, E. V. & Killelea, D. R. Thermally selective formation of subsurface oxygen in Ag(111) and consequent surface structure. *ACS Catal.* **6**, 4640–4646 (2016).
14. Rocha, T. C. R. et al. The silver–oxygen system in catalysis: new insights by near ambient pressure X-ray photoelectron spectroscopy. *Phys. Chem. Chem. Phys.* **14**, 4554–4564 (2012).
15. Jones, T. E. et al. Thermodynamic and spectroscopic properties of oxygen on silver under an oxygen atmosphere. *Phys. Chem. Chem. Phys.* **17**, 9288–9312 (2015).
16. Jones, T. E. et al. The selective species in ethylene epoxidation on silver. *ACS Catal.* **8**, 3844–3852 (2018).
17. Lei, Y. et al. Increased silver activity for direct propylene epoxidation via subnanometer size effects. *Science* **328**, 224–228 (2010).
18. Leow, W. R. et al. Chloride-mediated selective electrosynthesis of ethylene and propylene oxides at high current density. *Science* **368**, 1228–1233 (2020).
19. Harriott, P. The oxidation of ethylene using silver on different supports. *J. Catal.* **21**, 56–65 (1971).
20. Rovida, G., Pratesi, F., Maglietta, M. & Ferroni, E. Chemisorption of oxygen on silver (111) surface. *Surf. Sci.* **43**, 230–256 (1974).
21. Bocklein, S., Gunther, S. & Wintterlin, J. High-pressure scanning tunneling microscopy of a silver surface during catalytic formation of ethylene oxide. *Angew. Chem. Int. Ed.* **52**, 5518–5521 (2013).
22. Böcklein, S. et al. Detection and quantification of steady-state ethylene oxide formation over an Ag(111) single crystal. *J. Catal.* **299**, 129–136 (2013).

23. Campbell, C. The selective epoxidation of ethylene catalyzed by Ag(111)—a comparison with Ag(110). *J. Catal.* **94**, 436–444 (1985).
24. Christopher, P. & Linic, S. Engineering selectivity in heterogeneous catalysis: Ag nanowires as selective ethylene epoxidation catalysts. *J. Am. Chem. Soc.* **130**, 11264–11265 (2008).
25. Christopher, P. & Linic, S. Shape- and size-specific chemistry of Ag nanostructures in catalytic ethylene epoxidation. *ChemCatChem* **2**, 78–83 (2010).
26. Grant, R. B. & Lambert, R. M. A single crystal study of the silver-catalysed selective oxidation and total oxidation of ethylene. *J. Catal.* **92**, 364–375 (1985).
27. Costina, I. et al. Combined STM, LEED and DFT study of Ag(100) exposed to oxygen near atmospheric pressures. *Surf. Sci.* **600**, 617–624 (2006).
28. Carlisle, C. I., King, D. A., Bocquet, M. L., Cerda, J. & Sautet, P. Imaging the surface and the interface atoms of an oxide film on Ag{111} by scanning tunneling microscopy: experiment and theory. *Phys. Rev. Lett.* **84**, 3899–3902 (2000).
29. Reichelt, R. et al. High-pressure STM of the interaction of oxygen with Ag(111). *Phys. Chem. Chem. Phys.* **9**, 3590–3599 (2007).
30. Jones, T. E. et al. Insights into the electronic structure of the oxygen species active in alkene epoxidation on silver. *ACS Catal.* **5**, 5846–5850 (2015).
31. Carbonio, E. A. et al. Are multiple oxygen species selective in ethylene epoxidation on silver? *Chem. Sci.* **9**, 990–998 (2018).
32. Jones, T. E. et al. Oxidation of ethylene on oxygen reconstructed silver surfaces. *J. Phys. Chem. C* **120**, 28630–28638 (2016).
33. Bukhtiyarov, V., Prosvirin, I. & Kvon, R. Study of reactivity of oxygen states adsorbed at a silver surface towards $C_2h_4$ by XPS, TPD and TPR. *Surf. Sci.* **320**, L47–L50 (1994).
34. van Santen, R. A. & de Groot, C. P. M. The mechanism of ethylene epoxidation. *J. Catal.* **98**, 530–539 (1986).
35. Bukhtiyarov, V. I., Boronin, A. I. & Savchenko, V. I. Stages in the modification of a silver surface for catalysis of the partial oxidation of ethylene: I. action of oxygen. *J. Catal.* **150**, 262–267 (1994).
36. Bukhtiyarov, V. I., Boronin, A. I., Prosvirin, I. P. & Savchenko, V. I. Stages in the modification of a silver surface for catalysis of the partial oxidation of ethylene: II. action of the reaction medium. *J. Catal.* **150**, 268–273 (1994).
37. Carbonio, E. A. et al. Adjusting the chemical reactivity of oxygen for propylene epoxidation on silver by rational design: the use of an oxyanion and Cl. *ACS Catal.* **13**, 5906–5913 (2023).
38. Chen, D., Kang, P.-L. & Liu, Z.-P. Active site of catalytic ethene epoxidation: machine-learning global pathway sampling rules out the metal sites. *ACS Catal.* **11**, 8317–8326 (2021).
39. Kokalj, A., Gava, P., Degironcoli, S. & Baroni, S. What determines the catalyst's selectivity in the ethylene epoxidation reaction. *J. Catal.* **254**, 304–309 (2008).
40. Huš, M. & Hellman, A. Ethylene epoxidation on Ag(100), Ag(110), and Ag(111): a Joint ab initio and kinetic monte carlo study and comparison with experiments. *ACS Catal.* **9**, 1183–1196 (2019).
41. Özbek, M. O., Önal, I. & van Santen, R. A. Ethylene epoxidation catalyzed by silver oxide. *ChemCatChem* **3**, 150–153 (2011).
42. Ozbek, M. O., Onal, I. & van Santen, R. A. Why silver is the unique catalyst for ethylene epoxidation. *J. Catal.* **284**, 230–235 (2011).
43. Chen, B. W. J., Wang, B., Sullivan, M. B., Borgna, A. & Zhang, J. Unraveling the synergistic effect of Re and Cs promoters on ethylene epoxidation over silver catalysts with machine learning-accelerated first-principles simulations. *ACS Catal.* **12**, 2540–2551 (2022).
44. Xu, H., Zhu, L., Nan, Y., Xie, Y. & Cheng, D. Revisit the role of metal dopants in enhancing the selectivity of Ag-catalyzed ethylene epoxidation: optimizing oxophilicity of reaction site via cocatalytic mechanism. *ACS Catal.* **11**, 3371–3383 (2021).
45. Li, H., Cao, A. & Nørskov, J. K. Understanding trends in ethylene epoxidation on group IB metals. *ACS Catal.* **11**, 12052–12057 (2021).
46. Huš, M. et al. Going beyond silver in ethylene epoxidation with first-principles catalyst screening. *Angew. Chem. Int. Ed.* **62**, e202305804 (2023).
47. Li, W. X., Stampfl, C. & Scheffler, M. Why is a noble metal catalytically active? The role of the O–Ag interaction in the function of silver as an oxidation catalyst. *Phys. Rev. Lett.* **90**, 256102 (2003).
48. Stierle, A., Costina, I., Kumaragurubaran, S. & Dosch, H. In situ X-ray diffraction study of Ag(100) at ambient oxygen pressures. *J. Phys. Chem. C* **111**, 10998–11002 (2007).
49. Wexler, R. B., Qiu, T. & Rappe, A. M. Automatic prediction of surface phase diagrams using ab lnitio grand canonical monte carlo. *J. Phys. Chem. C* **123**, 2321–2328 (2019).
50. Behler, J. & Parrinello, M. Generalized neural-network representation of high-dimensional potential-energy surfaces. *Phys. Rev. Lett.* **98**, 146401 (2007).
51. Behler, J. Four generations of high-dimensional neural network potentials. *Chem. Rev.* **121**, 10037–10072 (2021).
52. Ma, S. & Liu, Z.-P. Machine learning for atomic simulation and activity prediction in heterogeneous catalysis: current status and future. *ACS Catal.* **10**, 13213–13226 (2020).
53. Liu, Q.-Y., Shang, C. & Liu, Z.-P. In situ active site for CO activation in Fe-catalyzed fischer–tropsch synthesis from machine learning. *J. Am. Chem. Soc.* **143**, 11109–11120 (2021).
54. Liu, Q.-Y., Chen, D., Shang, C. & Liu, Z.-P. An optimal Fe–C coordination ensemble for hydrocarbon chain growth: a full Fischer–Tropsch synthesis mechanism from machine learning. *Chem. Sci.* **14**, 9461–9475 (2023).
55. Shi, Y.-F., Kang, P.-L., Shang, C. & Liu, Z.-P. Methanol synthesis from $CO_2$/CO mixture on Cu–Zn catalysts from microkinetics-guided machine learning pathway search. *J. Am. Chem. Soc.* **144**, 13401–13414 (2022).
56. Li, J.-L., Li, Y.-F. & Liu, Z.-P. In situ structure of a Mo-doped Pt–Ni catalyst during electrochemical oxygen reduction resolved from machine learning-based grand canonical global optimization. *JACS Au* **3**, 1162–1175 (2023).
57. Jorgensen, M. S. et al. Atomistic structure learning. *J. Chem. Phys.* **151**, 054111 (2019).
58. Mortensen, H. L., Meldgaard, S. A., Bisbo, M. K., Christiansen, M.-P. & Hammer, B. Atomistic structure learning algorithm with surrogate energy model relaxation. *Phys. Rev. B* **102**, 075427 (2020).
59. Liu, J.-X., Lu, S., Ann, S.-B. & Linic, S. Mechanisms of ethylene epoxidation over silver from machine learning-accelerated first-principles modeling and microkinetic simulations. *ACS Catal.* **13**, 8955–8962 (2023).
60. Chen, D., Shang, C. & Liu, Z.-P. Machine-learning atomic simulation for heterogeneous catalysis. *NPJ Comput. Mater.* **9**, 1–9 (2023).
61. Chen, D., Shang, C. & Liu, Z.-P. Automated search for optimal surface phases (ASOPs) in grand canonical ensemble powered by machine learning. *J. Chem. Phys.* **156**, 094104 (2022).
62. Shang, C. & Liu, Z.-P. Stochastic surface walking method for structure prediction and pathway searching. *J. Chem. Theory Comput.* **9**, 1838–1845 (2013).
63. Huang, S.-D., Shang, C., Zhang, X.-J. & Liu, Z.-P. Material discovery by combining stochastic surface walking global optimization with a neural network. *Chem. Sci.* **8**, 6327–6337 (2017).
64. Huang, S.-D., Shang, C., Kang, P.-L. & Liu, Z.-P. Atomic structure of boron resolved using machine learning and global sampling. *Chem. Sci.* **9**, 8644–8655 (2018).
65. Huang, S.-D., Shang, C., Kang, P.-L., Zhang, X.-J. & Liu, Z.-P. LASP: fast global potential energy surface exploration. *WIREs Comput. Mol. Sci.* **9**, e1415 (2019).

66. Schnadt, J. et al. Experimental and theoretical study of oxygen adsorption structures on Ag(111). *Phys. Rev. B* **80**, 075424 (2009).
67. Van den Hoek, P. J., Baerends, E. J. & Van Santen, R. A. Ethylene epoxidation on silver(110): the role of subsurface oxygen. *J. Phys. Chem.* **93**, 6469–6475 (1989).
68. Xu, Y., Greeley, J. & Mavrikakis, M. Effect of subsurface oxygen on the reactivity of the Ag(111) surface. *J. Am. Chem. Soc.* **127**, 12823–12827 (2005).
69. Kang, P.-L., Shang, C. & Liu, Z.-P. Glucose to 5-hydroxymethylfurfural: origin of site-selectivity resolved by machine learning based reaction sampling. *J. Am. Chem. Soc.* **141**, 20525–20536 (2019).
70. Linic, S. & Barteau, M. A. Control of ethylene epoxidation selectivity by surface oxametallacycles. *J. Am. Chem. Soc.* **125**, 4034–4035 (2003).
71. Jones, G. S., Mavrikakis, M., Barteau, M. A. & Vohs, J. M. First synthesis, experimental and theoretical vibrational spectra of an oxametallacycle on a metal surface. *J. Am. Chem. Soc.* **120**, 3196–3204 (1998).
72. Linic, S., Piao, H., Adib, K. & Barteau, M. A. Ethylene epoxidation on Ag: identification of the crucial surface intermediate by experimental and theoretical investigation of its electronic structure. *Angew. Chem., Int. Ed.* **43**, 2918–2921 (2004).
73. van Hoof, A. J. F., Hermans, E. A. R., van Bavel, A. P., Friedrich, H. & Hensen, E. J. M. Structure sensitivity of silver-catalyzed ethylene epoxidation. *ACS Catal.* **9**, 9829–9839 (2019).
74. Pu, T. et al. Nature and reactivity of oxygen species on/in silver catalysts during ethylene oxidation. *ACS Catal.* **12**, 4375–4381 (2022).
75. Liu, C. et al. Computational and experimental insights into reactive forms of oxygen species on dynamic Ag surfaces under ethylene epoxidation conditions. *J. Catal.* **405**, 445–461 (2022).
76. Alzahrani, H. A. & Bravo-Suárez, J. J. In situ Raman spectroscopy study of silver particle size effects on unpromoted Ag/α-Al2O3 during ethylene epoxidation with molecular oxygen. *J. Catal.* **418**, 225–236 (2023).
77. Linic, S. & Barteau, M. A. Construction of a reaction coordinate and a microkinetic model for ethylene epoxidation on silver from DFT calculations and surface science experiments. *J. Catal.* **214**, 200–212 (2003).
78. Stegelmann, C., Schiodt, N. C., Campbell, C. T. & Stoltze, P. Microkinetic modeling of ethylene oxidation over silver. *J. Catal.* **221**, 630–649 (2004).
79. Byrne, G. D. & Hindmarsh, A. C. A Polyalgorithm for the numerical solution of ordinary differential equations. *ACM Trans. Math. Softw.* **1**, 71–96 (1975).
80. Johansson, F. et al. mpmath: a Python library for arbitrary-precision floating-point arithmetic (2017). http://mpmath.org/
81. Teržan, J., Huš, M., Likozar, B. & Djinović, P. Propylene epoxidation using molecular oxygen over copper- and silver-based catalysts: a review. *ACS Catal.* **10**, 13415–13436 (2020).
82. Kresse, G. & Furthmüller, J. Efficient iterative schemes for ab initio total-energy calculations using a plane-wave basis set. *Phys. Rev. B* **54**, 11169–11186 (1996).
83. Kresse, G. & Joubert, D. From ultrasoft pseudopotentials to the projector augmented-wave method. *Phys. Rev. B* **59**, 1758–1775 (1999).
84. Perdew, J. P., Burke, K. & Ernzerhof, M. Generalized gradient approximation made simple. *Phys. Rev. Lett.* **77**, 3865–3868 (1996).
85. Grimme, S., Antony, J., Ehrlich, S. & Krieg, H. A consistent and accurate ab initio parametrization of density functional dispersion correction (DFT-D) for the 94 elements H–Pu. *J. Chem. Phys.* **132**, 154104 (2010).
86. Lide, R. D. *CRC Handbook of Chemistry and Physics* (CRC Press, 2015).
87. Hoflund, G. B., Hazos, Z. F. & Salaita, G. N. Surface characterization study of Ag, AgO, and Ag2O using x-ray photoelectron spectroscopy and electron energy-loss spectroscopy. *Phys. Rev. B* **62**, 11126–11133 (2000).
88. van Hoof, A. J. F., van der Poll, R. C. J., Friedrich, H. & Hensen, E. J. M. Dynamics of silver particles during ethylene epoxidation. *Appl. Catal. B-Environ.* **272**, 118983 (2020).

## Acknowledgements

This work received financial support from the National Science Foundation of China (12188101, 22033003, 91945301, 91745201, 92145302, 22122301 and 92061112), Fundamental Research Funds for the Central Universities (20720220011) and the Tencent Foundation for XPLORER PRIZE.

## Author contributions

Z.-P.L. conceived the project and guided the research. D.C. designed and performed the theoretical simulations. L.C. designed and performed the experiments. Q.-C.Z. helped on the experiments. Z.-X.Y. helped on the code development and data analysis for the simulation of infra-red spectrum, C.S. helped on the code development. D.C. and L.C. drafted the manuscript. All authors discussed the manuscript and agreed with the content.

## Competing interests

The authors declare no competing interests.

## Additional information

**Supplementary information** The online version contains supplementary material available at https://doi.org/10.1038/s41929-024-01135-2.

**Correspondence and requests for materials** should be addressed to Zhi-Pan Liu.

**Peer review information** *Nature Catalysis* thanks Marc-Olivier Coppens and the other, anonymous, reviewer(s) for their contribution to the peer review of this work.